POLITECNICO DI TORINO
Repository ISTITUZIONALE

Plug-in, Direct Flux Vector Control of PM Synchronous Machine Drives

(Article begins on next page)

19 October 2024

Plug-in, Direct Flux Vector Control
of PM Synchronous Machine Drives

Gianmario Pellegrino   Barbara Boazzo
Dept. of Energy
Politecnico di Torino, Turin, Italy

Thomas M. Jahns
Dept. of Electrical and Computer Engineering
UW – Madison, Madison, WI   USA

Abstract— **A general-purpose control algorithm is proposed for permanent magnet (PM) synchronous machine drives based on the principles of Direct Flux Vector Control. The algorithm does not require regulators tuning, and it is tailored to different machines automatically via identification of the stator resistance and flux linkage tables. The model parameters are identified via a preliminary self-commissioning procedure that can be integrated into the standard drive firmware with no need for extra hardware or off-line manipulation. The combination of the control and self-commissioning algorithms forms a "plug-in" controller, meaning a controller that is capable of exploiting the full drive capabilities with no prior knowledge of the PM machine in use. Experimental results are reported for two prototype concentrated-winding PM machines designed for traction applications, one with a surface-mounted PM rotor and the other with an Interior PM rotor.**

I.   INTRODUCTION

High-performance salient-pole permanent magnet (PM) synchronous machine drives are widely adopted in modern energy conversion and motion control applications [1-3]. Such high torque/power-density machines are usually custom-designed to meet demanding performance requirements and operate in highly saturated conditions. Under these conditions, the magnetic model of the machines can become highly nonlinear, experiencing saturation also at partial-load and cross-saturation between the PM axis (d) and the quadrature axis (q). As a result, the basic three-parameter magnetic model (L_d, L_q, λ_m) is not sufficient for the characterization and control of high-torque-density and large-speed-range PM machines that require inductance mapping/adaptation and cumbersome data manipulation.

The model-dependency of these high-performance machines has hindered their adoption for general-purpose commercial products where it is difficult to standardize their control, and where engineers are accustomed to dealing with the reduced identification burden of modern induction machine or PM servomotor drives. The objective of this work is to develop an automatic means of performing the control calibration of any PM synchronous machine, opening the door to their wider commercial acceptance.

Reviewing the literature of PM machine controls, current vector control is well established and widely used, but it is heavily model-dependent in cases where the flux-weakening-speed operating region is important. In addition to knowledge of the machine model, major manipulation is often required to build multi-dimensional look-up tables [4] for the flux-weakening zone. Simpler model-independent methods are frequently applied [5-6], but they deliver much lower performance. Furthermore, none of these techniques includes

the maximum-torque-per-volt (MTPV) limited speed region, even though this is important in overloaded machines, such as the ones intended for traction and aerospace applications [7]. The control techniques based on direct control of the flux linkage vector, such as direct torque control (DTC) and direct-flux vector control (DFVC) [8,9], deal with the flux-weakening region much more easily in a model-independent manner. However, they still require knowledge of the machine model for flux orientation and also for maximum-torque-per-Amp operation [9,10].   This machine model knowledge is also required for predictive algorithms such as deadbeat control [11]. Because of this need for machine model knowledge, the existing control techniques require machine commissioning to acquire the necessary machine parameters, sometimes involving heavy model manipulation.

This paper proposes a plug-in control scheme that is suitable for general use with three-phase PM synchronous machine drives. The term "plug-in" indicates that the algorithm is self-adapting to the controlled machine with no need for model manipulation or even external calibration. The control scheme, based on DFVC, is completed here with an automatic machine commissioning procedure, with minimum impact in terms of time, need for equipment, or perturbation of the machine temperature.

The magnetic model self-identification (MMSI) procedure that is presented in this paper generates the tables of machine parameters directly in the form that is required by the controller, with no need for post-processing. The need for further parameter tuning is eliminated by the predictive implementation of DFVC presented in [12].   Another advantage of the predictive implementation is that it has a robust dynamic response over the complete torque-speed operating region, whereas regulator-based controllers require the adaptation of the proportional and integral gains throughout the flux-weakening operating area [13]. Power converter identification is also automatic [14].

Experimental results are provided using test results for two concentrated-winding PM machines designed for traction applications. The effects of parameters detuning is addressed, and experimentally evaluated. The two machines under test have the same 12-slot stator and exchangeable 10 pole pair rotors, one with surface-mounted PMs (SPM) and the other with interior PMs (IPM) [17].

II.   PREDICTIVE DIRECT FLUX VECTOR CONTROL

The DFVC algorithm is based on the machine voltage model (1), expressed in the stator flux linkage reference frame (ds,qs) that is defined in Fig. 1a. In (1), the control state variables λ and δ represent the flux linkage amplitude and the

load angle, respectively. The angle δ is defined in Fig. 1 as the angle between the stator flux linkage and the rotor *d*-axis. The *ds*-axis direct voltage component controls the flux amplitude in closed-loop, while the *qs*-axis quadrature voltage controls the load angle δ.

$$\begin{cases} v_{ds} = R_s \cdot i_{ds} + \dfrac{d\lambda}{dt} \\ v_{qs} = R_s \cdot i_{qs} + \left(\dfrac{d\delta}{dt} + \omega\right) \cdot \lambda \end{cases} \tag{1}$$

The current model is conveniently expressed in the rotor synchronous *dq* reference frame:

$$\begin{cases} \lambda_d = L_d(i_d, i_q) \cdot i_d + \lambda_m \\ \lambda_q = L_q(i_d, i_q) \cdot i_q \end{cases} \tag{2}$$

The direct and cross-dependences of the inductances on the current components are evident in (2). Cross saturation has no dedicated L_{dq}, L_{qd} terms in these equations, but its effects are implicitly taken into account in the form of L_d and L_q variations with the cross-current components i_a and i_d, respectively. λ_m is the open circuit flux linkage, originated by the PMs. The torque expression as a function of the state variables λ and δ is:

$$T = \frac{3}{2}p\left(\frac{\lambda\lambda_m}{L_d}\sin(\delta) - \frac{\lambda^2}{2L_q}\left(\frac{L_q}{L_d} - 1\right)\sin(2\delta)\right) \tag{3}$$

More conveniently, the DFVC control algorithm's foundation is the alternative torque expression (4), where i_{qs} is redefined as the quadrature current component in flux coordinates:

$$T = \frac{3}{2}p \cdot \lambda \cdot i_{qs} \tag{4}$$

The torque control block diagram is provided in Fig. 1b. The construction of the λ^* and $i_{qs}{}^*$ reference values from the torque reference T^* follows (4). The converter current and voltage limits are included in the convenient form of *two saturation blocks*. The saturation of i_{qs} bounds the current

amplitude, while the speed-dependent saturation of the flux linkage amplitude insures that the inverter maximum voltage limit is respected. This is a parameter-independent way to handle the flux-weakening speed region, making it insensitive to the machine parameters [9].

The closed-loop control of λ and i_{qs} is performed here in a predictive, model-based manner, taking advantage of explicit inverse machine equations to relate the flux and current errors to the corresponding voltage command values. The load angle error comes from the key equation (5), whose inputs are both the flux amplitude and *qs*-current errors (standing for the coupling between the *ds*- and the *qs*- control axes):

$$\Delta\hat{\delta}^* = \frac{\Delta i_{qs}^* + K \cdot \Delta\lambda^*}{H \cdot \cos[\hat{\delta}(k+1)] - 2K \cdot \cos[2 \cdot \hat{\delta}(k+1)] \cdot \hat{\lambda}(k+1)} \tag{5}$$

$$H = \frac{\lambda_m}{\hat{L}_d(k)} \qquad K = \frac{\hat{L}_q(k) - \hat{L}_d(k)}{2 \cdot \hat{L}_d(k) \cdot \hat{L}_q(k)} \tag{6}$$

The mathematical derivation of (5) is provided in the Appendix. Other than being a function of the two control errors $\Delta\lambda^*$ and Δi_{qs}^*, the load angle error is also a function of the magnetic model parameters $L_d(i_d, i_q)$, $L_q(i_d, i_q)$, λ_m, and the observed state variables $\hat{\lambda}$ and $\hat{\delta}$. All these state-dependent quantities are outputs of the **Predictive Flux and Current Observer** block visible at the bottom of Fig. 1b which is the key block of the proposed control scheme.

The "predictive" nature of the observer refers to the fact that some of the observed quantities (ˆ) are discrete time increments (*k*+1) based on calculations at the preceding time step (*k*) in a predictive fashion, where (*k*) represents the current computational time instant of the real-time digital controller. The prediction at time (*k*+1) is mandatory in order to compensate for the actuation delay of the digital controller. Without it, the control response is chattery and oscillatory [11,16-17].
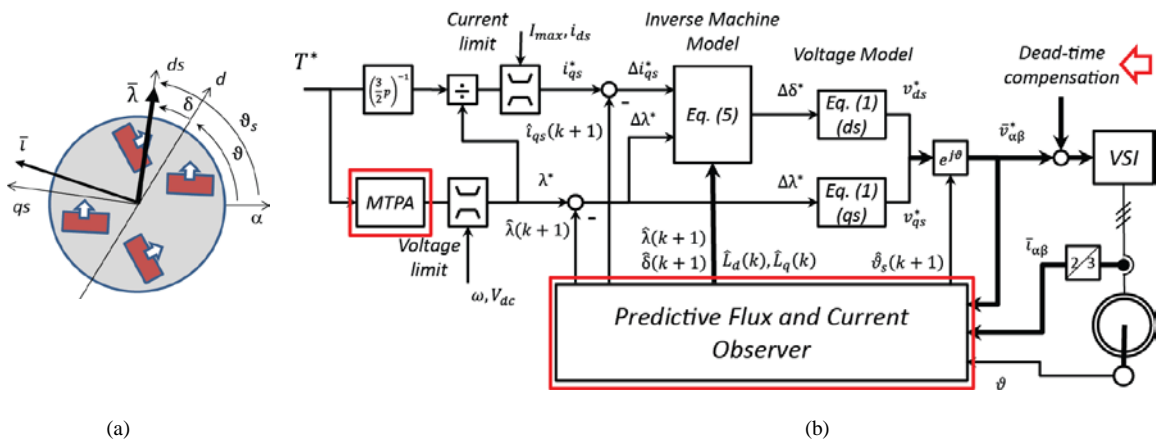

(a)   (b)

Figure 1.   a) Definition of the flux-oriented reference frame (*ds, qs*) for a generic PM motor rotor. b) Block diagram of the proposed predictive DFVC algorithm. The VSI block represents the "Voltage Source Inverter".

Returning to Fig. 1b, the reference voltage vector in (*ds, qs*) components follows readily from the flux linkage amplitude and phase errors $\Delta\lambda^*$ and $\Delta\delta^*$, through the discrete form of (1).

Dealing with the model parameters necessary to the control, the red squares in Fig. 1b identify the blocks where knowledge of the magnetic model is needed. More specifically, these include the flux observer and the maximum-torque-per-Ampere (MTPA) look-up table, used to generate the flux amplitude reference λ^* from the torque reference T^* according to the minimum copper loss strategy. The implementation of those two blocks is addressed in the following sections.

A. Predictive Flux and Current Observer

The discrete-time block diagram of the predictive observer is represented in Fig. 2. The sequence of the operations is:

1) to calculate the flux linkage at time (*k*);
2) to evaluate the equivalent inductances applying the inverse of (2);
3) to predict the current at the next time step (*k+1*) using the voltage model;
4) to predict the flux linkage at time (*k+1*) using once more the magnetic model (2).

The first operation is carried out using a closed-loop stator flux observer, where the current-to-flux model in *dq* rotor synchronous coordinates is best suited to the low-speed operating region, and the voltage model in αβ coordinates works well for the higher-speed range [9, 11]. The crossover angular frequency between the low- and high-speed models is set by the observer feedback gain *g* (electrical rad/s). The control reference voltage signals are used as the observer inputs for estimating the motor voltages. The rotor position comes from an encoder. The output of the first observer stage is the estimated flux linkage vector in *dq* coordinates at the present time instant $\hat{\lambda}_{dq}(k)$. From that, the *dq* inductances are estimated according to (7):

$$\hat{L}_d(k) = \frac{\hat{\lambda}_d(k)-\lambda_m}{i_d(k)} \qquad \hat{L}_q(k) = \frac{\hat{\lambda}_q(k)}{i_q(k)} \qquad (7)$$

As explained for equation (2), the inductances in (7) also include the effect of cross-saturation that is evaluated instant by instant according to the present magnetic state of the machine.

The third operation is to predict the *dq* current components at time (*k+1*) via discrete-time integration of the first-order differential equations (8), using the just-calculated inductance values (7):

$$\begin{cases} \hat{L}_d \, \frac{di_d}{dt} = v_d - R_s i_d + \omega\lambda_q \\ \hat{L}_q \, \frac{di_q}{dt} = v_q - R_s i_q - \omega\lambda_d \end{cases} \qquad (8)$$

Figure 2 reports the first-order approximated discrete form of (8). Finally, the *dq* flux linkage components at time (*k+1*) are calculated from the predicted current components using (2). The amplitude and phase angles δ and θ_s of the flux linkage vector in the *dq* and αβ reference frames, respectively, are calculated using simple mathematics.

The current extrapolation equations (8) contain an approximation, related to the use of apparent inductances (7) instead of incremental ones. However, it turns out that using the apparent inductances to solve (8) in real-time is accurate enough for the purpose of this analysis. The torque step response tests reported in section IV show that the modelling imprecision does not harm the smoothness and steady-state exactness of the control response.

The flux look-up table ("Flux LUT") block, highlighted with a red box in Fig. 2, is the one requiring the most intense machine identification effort of the entire control scheme. Section III addresses how the flux linkage look-up tables can be generated automatically.
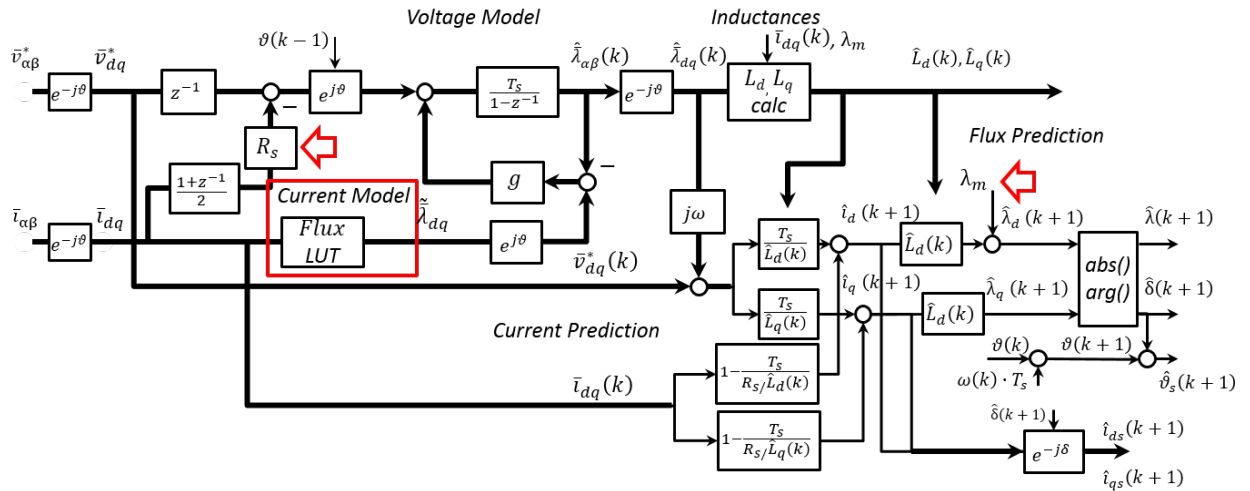

Figure 2. Predictive stator flux linkage and current observer.

One last word about how incremental inductances could be included in the algorithm and used in (8). These could be obtained in real-time by differentiation of the flux linkage LUTs. However, the differentiation of the tables would easily introduce discretization noise into the control loops, proportionally to the spacing of the i_d, i_q mesh underpinning the LUTs. Tests on different PM machine types have discouraged this solution.

III. MACHINE AND INVERTER SELF-IDENTIFICATION

The control algorithm summarized by the block diagrams in Figs. 1b and 2 has the appealing feature of segregating its dependencies on the machine and inverter parameters into a very limited set of blocks. Considering first the required machine parameters, the blocks in Fig. 2 that must be updated when switching from one machine to another are the *machine resistance R_s*, the *Current to Flux Linkage Look Up Tables* (Flux LUT) and the *PM flux linkage λ_m* that is anyway included into the Flux LUT.

In Fig. 1b, the only parameter dependent block is the *MTPA look-up table*. The inverter parameters are summarized by the "*Dead-Time Compensation*" input term in Fig. 1b. An accurate commissioning procedure is very important for this DFVC control algorithm in order to secure the required machine and inverter parameters.

The inverter self-identification and compensation technique described in [14] is used here, which also includes identification of the initial machine resistance. Other techniques reported in the literature such as [15] are also effective.

The machine electromagnetic model is provided by a new self-identification procedure that is referred to here as Magnetic Model Self-Identification (MMSI), described in the next subsection.

The MTPA look-up table can be derived from manipulation of the electromagnetic curves generated by the MMSI procedure or by means of one of the MTPA commissioning techniques reported in the literature [18-19]. Experience to date with the DFVC algorithm using PM machines of very different types and saliency characteristics indicates that the control performance, evaluated in terms of Joule loss per torque and torque dynamic response, is not very sensitive to the accuracy of the MTPA table. That is, it is not critical in most applications to identify the exact MTPA curve, but only the no-load and rated-torque flux amplitude reference values [20].

The MTPA table identification was accomplished here using a dedicated, automatic commissioning session that is very similar to the MMSI procedure, but further discussion of this topic is beyond the scope of this paper.

A. Flux Linkage Look-up Tables

The flux linkage look-up tables are in the form:

$$\begin{cases} \lambda_{d,LUT}(i,j) = \lambda_d\big(i_{d,i}, i_{q,j}\big) \\ \lambda_{q,LUT}(i,j) = \lambda_q\big(i_{d,i}, i_{q,j}\big) \end{cases} \quad (9)$$

with i and j going from one to ten in the examples, corresponding to a 10 per 10 square grid of i_d, i_q test couples covered during the identification procedure. As an example of the LUT's organization, the experimental flux linkage data for the IPM machine under test are reported in Fig. 3.
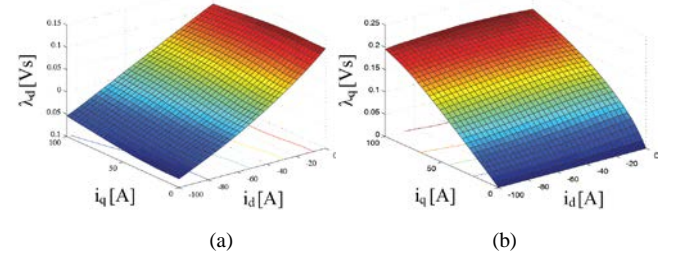

Figure 3. Experimental *dq* flux linkage versus *dq* current components based on measurements for the tested IPM machine. a) *d*-axis flux surface, b) *q*-axis flux surface.

In this case, the flux linkages were estimated off-line at constant speed, imposed by a closed-loop controlled dynamometer rig [21-22]. The surfaces in Figs. 3a) and 3b) were interpolated off-line using a grid of 32 x 32 elements. The square identification grid, qualitatively depicted in Fig. 4a, is used here for a comfortable representation of the flux linkage tables and curves. However, in real world applications the inverter current limit would suggest to use a circular current domain, doable with little modifications to the procedures described in the paper. The circular current limit is indicated with a red circle in Fig. 4a.

B. Magnetic Model Self-Identification [23]

For the MMSI procedure, the machine has its shaft free to rotate and it is accelerated and decelerated using fixed current commands (i_d, i_q) and closed-loop vector control. Starting from zero speed, one of the set-points of the grid $i_d^*(i), i_q^*(j)$ is imposed and the machine accelerates. Any (i_d, i_q) condition corresponds to a steady flux linkage vector in *dq* coordinates, as suggested in Fig. 4b.

Due to the presence of steady *dq* current and a flux linkage vectors, the machine starts to accelerate at constant rate, under the constant electromagnetic torque imposed by the current controller. In such conditions, the *dq* flux linkage vector components can be derived from the back-emf estimate, once more in *dq* coordinates, according to the "quasi-steady-state" equation:

$$\bar{v}_{dq} = R_s \bar{\imath}_{dq} + \frac{d\bar{\lambda}_{dq}}{dt} + j\omega\bar{\lambda}_{dq} = R_s \bar{\imath}_{dq} + j\omega(t) \cdot \bar{\lambda}_{dq} \quad (10)$$

where ω(t) is the electrical speed, R_s is the stator resistance and v_d, v_q are the voltage vector components. The flux derivative term was dropped in (10) due to the constant flux linkage components. This assumption is strictly true under the conditions $i_d = i_d^*$, $i_q = i_q^*$, i.e., after the very short initial electrical transient. The flux linkage components are estimated accordingly, from the machine voltages, the current measurements, and the electrical speed:

$$\lambda_d = \frac{v_q(t) - R_s i_q}{\omega(t)} \qquad \lambda_q = -\frac{v_d(t) - R_s i_d}{\omega(t)} \quad (11)$$

The time-dependence of the voltage and speed terms in (10) and (11) reflects the fact that the speed and the voltage signals are varying during the test. Conversely, the current and flux linkage components are virtually steady.
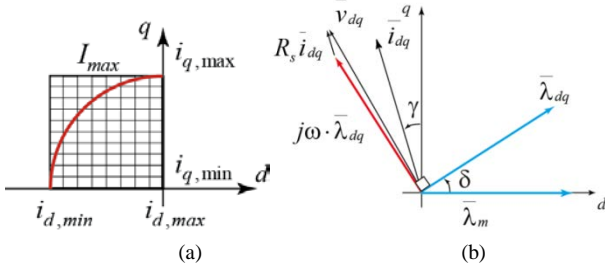

Figure 4. a) Sample current plane of a PM synchronous machine illustrating the type of current vector grid used for the MMSI identification procedure; b) steady-state vector diagram of a PM synchronous machine.
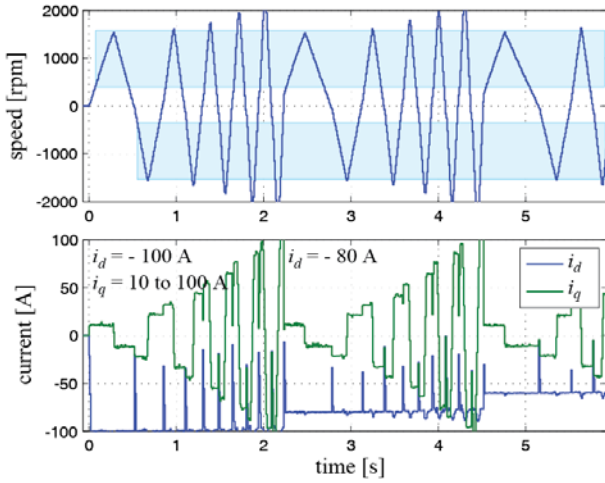

Figure 5. Speed and dq current waveforms during the MMSI of the SPM machine. The current pattern is i_d from -100A to 0 A, i_q from 10 A to 100A, both with step 10 A.

The speed information in (11) is derived from the shaft position sensor, and the voltage vector comes from the voltage commands, with the inverter error component compensated. The stator resistance voltage must also be compensated. Those three aspects are discussed later in this section.

C. MMSI Routine and Data Manipulation

Figure 5 shows an example MMSI routine. The measured speed and the dq currents are displayed. The IPM machine-under-test is initially controlled at i_d = -100 A and i_q 10 A, which is the first test point of the current grid. The shaded speed range between 500 rpm and 1500 rpm indicates the time window where the flux linkage evaluation takes place, both during acceleration and deceleration phases. With reference any of the $i_d^*(i)$, $i_q^*(j)$ combinations of Fig. 5, the flux linkage in estimated instantaneously and accumulated into two scalar variables $\tilde{\lambda}_{d,acc}$ and $\tilde{\lambda}_{q,acc}$, at all time-instants of the speed window:

$$\begin{cases} \tilde{\lambda}_{d,acc}(k) = \tilde{\lambda}_{d,acc}(k-1) + \frac{v_{q*}(k) - R_s i_{q,j}(k)}{\omega(k)} \\ \tilde{\lambda}_{q,acc}(k) = \tilde{\lambda}_{q,acc}(k-1) - \frac{v_{d*}(k) - R_s i_{d,i}(k)}{\omega(k)} \end{cases} \quad (12)$$

Where (k) and (k-1) indicate the current sampling time and the precedent one, respectively. At the exit of the time window (1500 rpm in acceleration, 500 rpm in deceleration), the accumulated estimate is divided by the number of accumulated samples n, corresponding to the sampling time instances occurred between 500 rpm and 1500 rpm:

$$\begin{cases} \lambda_{d,LUT}(i,j) = \frac{\tilde{\lambda}_{d,acc}(n)}{n} \\ \lambda_{q,LUT}(i,j) = \frac{\tilde{\lambda}_{q,acc}(n)}{n} \end{cases} \quad (13)$$

In other words, the instantaneous flux linkage estimates are averaged over time for the sake of noise rejection. Equation (14) is equivalent to (13):

$$\begin{cases} \lambda_{d,LUT}(i,j) = \frac{1}{n} \cdot \sum_{k=1}^{n} \frac{v_{q*}(k) - R_s i_{q,j}(k)}{\omega(k)} \\ \lambda_{q,LUT}(i,j) = \frac{1}{n} \cdot \sum_{k=1}^{n} - \frac{v_{d*}(k) - R_s i_{d,i}(k)}{\omega(k)} \end{cases} \quad (14)$$

D. Motor-Brake Average

A further improvement of the flux estimate robustness is obtained if the deceleration phase is handled with the symmetrical current condition $i_d^*(i), -i_q^*(j)$. In this way, the flux linkage in deceleration is symmetrical to the one in acceleration, with the same d- component and opposite q-component. The procedure described by (12) and (13) is repeated in deceleration so to make a second flux estimate available. The *mot* and *br* vectors are defined: *mot*, for *motor* i.e. acceleration, *br*, for *brake*, i.e. deceleration:

$$\bar{\iota}_{dq,mot} = i_d + j \cdot i_q , \ \bar{\iota}_{dq,br} = i_d - j \cdot i_q \quad (15a)$$

$$\bar{\lambda}_{dq,mot} = \lambda_d + j \cdot \lambda_q , \ \bar{\lambda}_{dq,br} = \lambda_d - j \cdot \lambda_q \quad (15b)$$

The average between the *mot* and *brake* estimates becomes the final LUT entry:

$$\begin{cases} \lambda_{d,LUT}(i,j) = \frac{\lambda_{d,LUT,mot} + \lambda_{d,LUT,br}}{2} \\ \lambda_{q,LUT}(i,j) = \frac{\lambda_{q,LUT,mot} - \lambda_{q,LUT,br}}{2} \end{cases} \quad (16)$$

The *motor + brake* test is repeated over the whole (i_d, i_q) identification grid. The *motor + brake* average improves the robustness of the MMSI procedure against imprecise compensation of inverter error and series resistance voltage. For example, a resistance estimate error $\Delta R_s = \tilde{R}_s - R_s$ produces a flux estimate error after application of (11). The instantaneous estimate therefore is:

$$\tilde{\lambda}_d = \frac{v_q(t) - \tilde{R}_s i_q}{\omega(t)} = \lambda_d - \frac{\Delta R_s i_q}{\omega(t)} \quad (17a)$$

$$\tilde{\lambda}_q = -\frac{v_d(t) - \tilde{R}_s i_d}{\omega(t)} = \lambda_q + \frac{\Delta R_s i_d}{\omega(t)} \quad (17b)$$

Where λ_d, λ_q are the correct flux linkages and $\tilde{\lambda}_d$, $\tilde{\lambda}_q$ are the estimates evaluated by the microcontroller. After time

average (14), the flux estimate error evidenced in (17) is also averaged:

$$\tilde{\lambda}_{d,LUT,mot} = \lambda_d - \frac{\Delta R_s i_q}{\omega_{avg}} \ , \ \tilde{\lambda}_{q,LUT,mot} = \lambda_q + \frac{\Delta R_s i_d}{\omega_{avg}} \quad (18)$$

Where ω_{avg} is the average speed across the speed window used for data acquisition. The *brake* test has complex conjugate current and flux linkage vectors (15), therefore its flux linkage estimate after time-average (14) is:

$$\tilde{\lambda}_{d,LUT,br} = \lambda_d - \frac{\Delta R_s(-i_q)}{\omega_{avg}'} \ , \ \tilde{\lambda}_{q,LUT,br} = -\lambda_q + \frac{\Delta R_s i_d}{\omega_{avg}'} \quad (19)$$

Where ω_{avg}' is the speed average in deceleration. It is fair to assume that $\omega_{avg}' = \omega_{avg}$, since the speed window is the same for motoring and braking. Average between *mot* and *brake* (16) cancels the estimate error terms.

The same demonstration holds for non-correct compensation of the inverter voltage error: the fundamental component of the related flux linkage error is compensated by *motor* and *brake* average (16) as said, whereas higher order harmonics are preliminarily cancelled in the time average process (14).

The last comment about Fig. 5 is that positive and negative speed sides are alternated on purpose, during the MMSI routine. Such alternation is useful for detecting an encoder offset error. If the encoder offset is inaccurate, the LUTs will exhibit discontinuities that can be easily detected and used to correct the angular offset automatically. More details about automatic error detection can be found in [23].

E. Inverter and Stator Resistance Identification

The stator resistance and the inverter voltage error are identified with the off-line direct-current procedure described in [14]. The identification procedure is embedded into the drive control software and run once. The identification sequence consists of a sequence of dc pulses commanded along the *alpha* axis by means of a current controller. If necessary, a first dc current aligns the *d-* rotor axis to its zero position (*parking* stage). Another two dc pulses are used for the measurement of the stator resistance. Finally, a staircase of dc pulses is used to obtain the table of compensation values reported in Fig. 6, representing the non-linear inverter error (in Volts) as a function of the absolute value of each phase current. This look-up table is used to replace the traditional signum function-based compensation such as the one in [15], resulting in smoother current and flux linkage waveforms in the vicinity of the current zero crossings.
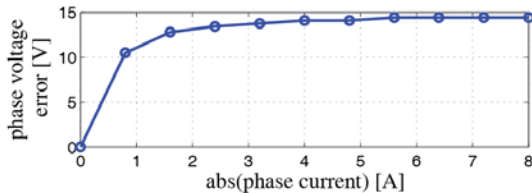

Figure 6. Look-up table for inverter error compensation.

F. Tuning of the Observer Gain

The tuning of the observer gain *g* is not critical. Values between 200 and 600 rad/s were tested with little effect on the final performance. As a result, it is possible to change the machine without the need for adjusting *g*, including the case of a new machine with a different number of poles. For the five-pole-pair machines under test, *g* set at 200 rad/s means that the cross-over between the low- and high-speed regimes occurs at 382 r/min; *g* = 600 rad/s increases it to 1146 r/min.

G. Effect of Temperature Variations over λ_m and R_s

The PM flux linkage λ_m used in (7) is one element of the flux linkage LUTs that comes from the MMSI session. It is known that this term varies inversely with the PM operating temperature, and this affects the output torque. The detuning of λ_m does not harm the DFVC stability, as confirmed by the experimental results. However, temperature variations produce a progressive torque estimate error, resulting in a degradation of the torque scale factor. For example, if the machine identification refers to room temperature conditions, then a torque overestimate is expected at rated temperature conditions because the actual torque will be lower than the one set by the controller. Unfortunately, such torque factor de-rating with temperature is not unusual in PM synchronous drives, regardless of the adopted control technique. Possible countermeasures include: 1) warming up the machine to the rated operating temperature prior to the MMSI procedure; or 2) using an online parameter observer, such as the one in [16]. The first alternative requires significant extra time but can be done automatically.

Dealing with temperature variation of the stator resistance, this can be re-estimated periodically when the drive stops with the two dc steps method described in section III.E. Alternatively, on-line adaptation techniques are reported in the literature [16] but they are not included in the presented implementation.

IV. EXPERIMENTAL VALIDATION

The tested machines are both rated for 55 kW (peak) and 30 kW continuous, with a maximum rotor speed of 14 krpm and a corner speed of 2800 r/min.

TABLE I. KEY PARAMETERS AND METRICS OF THE TWO TEST MACHINES

	IPM	SPM		IPM	SPM
Number of slots	12		Rated current [Apk]	113	109
Pole pairs (*p*)	5		Characteristic current [Apk]	50	87
Stator outer diameter	274		dc-link voltage [V]	320	
Stack length [mm]	73.4		Open-circuit voltage line to line [Vpk]	314	328
Airgap [mm]	0.73	1.85			
Rated speed [rpm]	2800		Inertia [kg m^2]	21·10^{-3}	21·10^{-3}
Rated Torque [Nm]	102		Type of cooling	liquid	

Figure 7. View of the test rig. The dSPACE 1103 PPC host computer is on the desk. The machine-under-test is in the red square to the right, connected to an induction machine dyno via an inline torquemeter (not visible). The red square to the left indentifies the power converters.
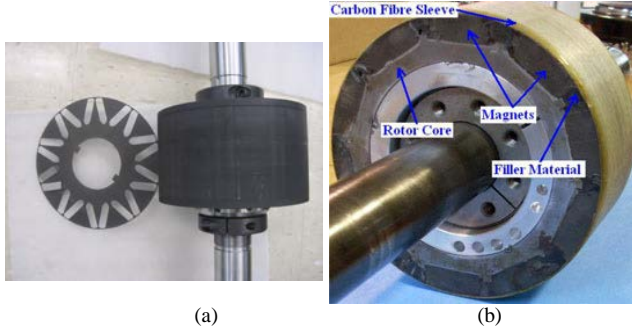

Figure 8. a) IPM machine rotor; b) SPM machine rotor [17].

More details about the two concentrated winding IPM machine can be found in [17] and in Table I. A view of the test rig is provided in Fig. 7. The inverters for the machine-under-test and the dyno machine are connected back-to-back, with an active front end supplying the common dc-link at a stable value of 313 Vdc. The rotors of the two machines are shown in Fig. 8.

A. Results of the MMSI stage

Parametric flux linkage curves plotted for the two test machine using data in the measured flux linkage LUTs are presented in Fig. 9. The correspondence with the same curves obtained using constant-speed identification is quite good, and more details on this topic can be found in [23]. In addition, the promising response characteristics of the predictive control when the MMSI output tables are adopted provide further confidence in their accuracy.

B. Torque Step and Speed Step Responses

The experimental results for the DFVC algorithm show the torque step response in different configurations. In Fig. 10, the response to a 30 Nm torque step is shown at 100 r/min for the two motors. The low per-unit speed level was chosen as an example of performance in the low-speed region where the flux observer relies on the flux linkage LUTs. Figure 10 demonstrates the good dynamic response of the control.
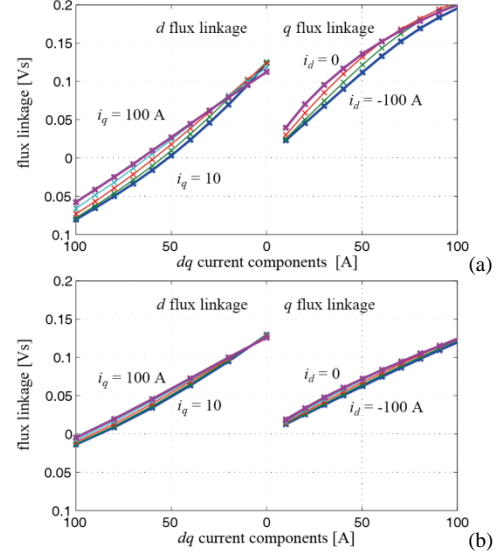

Figure 9. d- and q-axis flux linkage curves obtained from the MMSI procedure: a) for the IPM machine; b) for the SPM machine.
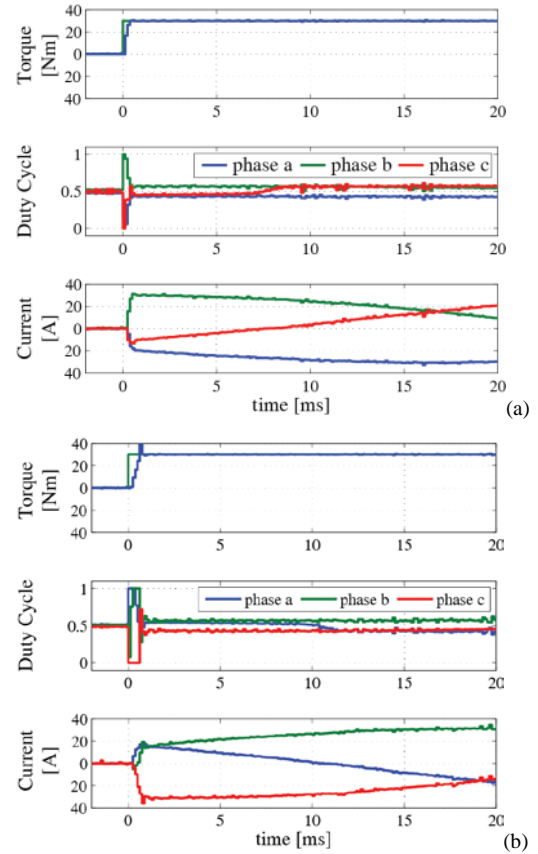

Figure 10. 0 to 30 Nm step response at 100 rpm. a) SPM motor; b) IPM motor. Top: estimated torque [Nm], Center: phase duty-cycles; Bottom: phase currents [A]
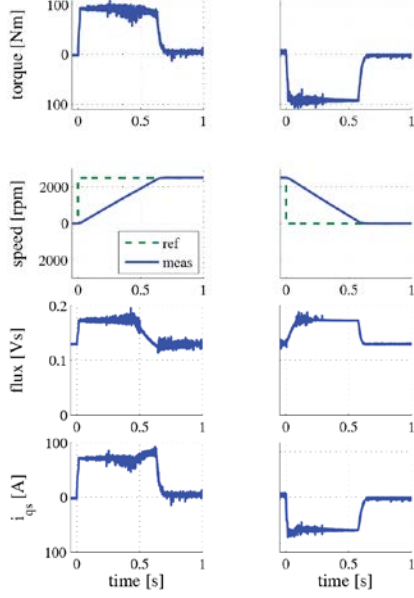
Figure 11. Response of the closed-loop speed control to a reference step from 0 to 2500 rpm and return. The torque signal is the observed torque.

The response of the IPM machine is slower than the SPM machine response due to the higher stator inductance and the correspondingly larger Vs-per-Nm variation. Once more, the smooth response of the model-based, predictive controller stands for the correctness of the MMSI obtained LUTs. If the magnetic model was not accurate enough, then the predictive controller would become inaccurate and chattery.

The response of the closed-loop speed control to a speed reference step is reported in Fig. 11 for the SPM machine. The transition into the flux-weakening speed region is visible in proximity of 2000 r/min from the reduction of the flux linkage amplitude. The corner speed is lower than the one listed in Table I because the ratings there refer to parallel connection of the two internal stator windings, whereas the results here have the two windings connected in series.

C. Detuning Effects

In Fig. 12a the inverter error compensation is turned off and the control becomes chattery, with large deviations of the PWM duty-cycle that propagate to all of the other variables. This undesirable behavior confirms the importance of this compensation as a mandatory feature.

The effect of detuning the key parameter λ_m is shown in Fig. 12b. Three torque step responses are shown overlaid for the IPM machine: one has the parameter set correctly and the other two have progressive overestimates of the control parameter to mimic the effects of heating of the machine (i.e., λ_m estimate greater than actual). The results show that the control is stable and smooth in all three cases. In the top plot the commanded 30 Nm is apparently delivered according to the observed torque. However, the *dq* current vector plot (bottom x-y plot) shows that the steady-state position of the current vector drifts to lower amplitude conditions (i.e. a

lower torque) progressively with the detuning. This is also confirmed by the torque meter display.

V. CONCLUSION

This work demonstrates the promising characteristics of the plug-in Direct Flux Vector Control algorithm (DFVC) for synchronous PM machine drives. The key contributions of the paper are the segregation of the converter and machine parameters in a limited set of blocks and in non-manipulated form, and the integration of the machine identification procedure into the control firmware. This Magnetic Model Self-Identification (MMSI) algorithm can help enabling the wider application of high performance PM machine drives in general-purpose commercial drives, thereby avoiding the need for custom-designed machines and custom-designed controllers for each new application. The MMSI procedure used in this paper has been validated in experiments, demonstrating its effectiveness. Results with two 55 kW (pk) IPM and SPM machines have exhibited promising dynamic characteristics. Parameters detuning and flux weakening operation have also been addressed and verified experimentally. Future efforts will be devoted to eliminating the need for an encoder or resolver and to the possibility of integrating standstill MMSI techniques, for those applications where the motor cannot be decoupled from the load.
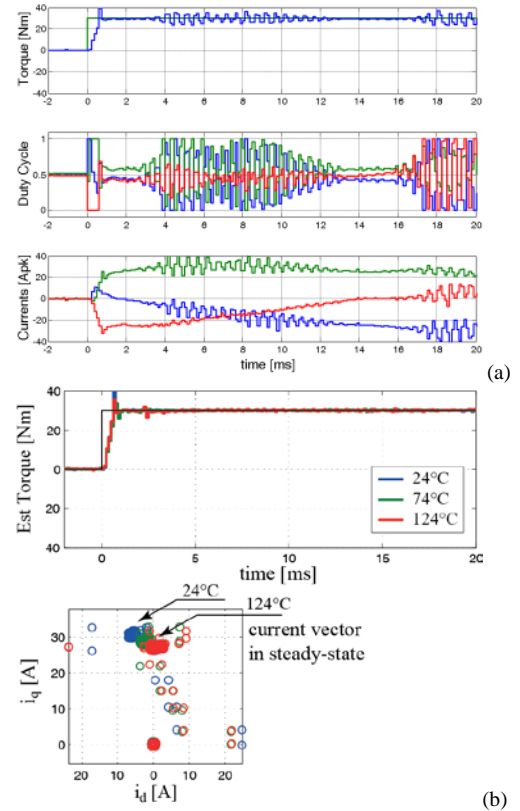

(a)

(b)

Figure 12. a) Same test of Fig. 9b, without dead-time compensation. b) Effect of overestimating the λ_m parameter by 10% and 20%, corresponding to mimic PM temperature values of 74°C and 124°C, respectively. Top: estimated torque, bottom: *dq* current vector trajectories.

APPENDIX - MATHEMATICAL DERIVATION OF EQUATION (5)

The *dq* magnetic model (2) is rotated by δ and referred to the stator field-oriented frame (*ds,qs*):

$$\begin{cases} \lambda = L_{ds} \cdot i_{ds} + L_{dqs} \cdot i_{qs} + \lambda_m \cos(\delta) \\ 0 = L_{dqs} \cdot i_{ds} + L_{qs} \cdot i_{qs} - \lambda_m \sin(\delta) \end{cases} \quad (1A)$$

The inductance terms L_{ds}, L_{ds} and L_{dqs} in the new reference frame depend on L_d and L_q and on the load angle δ:

$$\begin{bmatrix} L_{ds} & L_{dqs} \\ L_{dqs} & L_{qs} \end{bmatrix} = \begin{bmatrix} L_0 - \Delta L \cos(2\delta) & \Delta L \sin(2\delta) \\ \Delta L \sin(2\delta) & L_0 + \Delta L \cos(2\delta) \end{bmatrix} \quad (2A)$$

$$L_0 = \frac{L_d + L_q}{2} \qquad \Delta L = \frac{L_q - L_d}{2} \quad (3A)$$

The magnetic equations (1A) and (2A) are now manipulated to find the relationship between the control errors $\Delta\lambda$ and Δi_{qs} and the corresponding load angle variation $\Delta\delta$. By differentiating the two component equations of (1A), equations (4A) and (6A) are found, the former referring to the *ds* component of (1A), and the latter to the *qs* component.

$$\frac{di_{ds}}{dt} = A \cdot \frac{d\lambda}{dt} + B \cdot \frac{di_{qs}}{dt} + C \cdot \frac{d\delta}{dt} \quad (4A)$$

$$\begin{cases} A = \frac{1}{L_0 - \Delta L \cos(2\delta)} \\ B = -\frac{\Delta L \sin(2\delta)}{L_0 - \Delta L \cos(2\delta)} \\ C = -\frac{2\Delta L(\sin(2\delta) i_{ds} + \cos(2\delta) i_{qs}) - \lambda_m \sin(\delta)}{L_0 - \Delta L \cos(2\delta)} \end{cases} \quad (5A)$$

$$\frac{di_{ds}}{dt} = B' \cdot \frac{di_{qs}}{dt} + C' \cdot \frac{d\delta}{dt} \quad (6A)$$

$$\begin{cases} B' = -\frac{L_0 + \Delta L \cos(2\delta)}{\Delta L \sin(2\delta)} \\ C' = -\frac{2\Delta L(\cos(2\delta) i_{ds} - \sin(2\delta) i_{qs}) - \lambda_m \cos(\delta)}{\Delta L \sin(2\delta)} \end{cases} \quad (7A)$$

The time derivative of i_{ds} isolated on the left sides of both (4A) and (6A) so that it can be eliminated by equaling the right-hand sides of the two equations. After the simplification of di_{ds}/dt, the final equation (8A) contains the time derivatives of λ, i_{qs} and δ.

$$(C - C') \cdot \frac{d\delta}{dt} = (B' - B) \cdot \frac{di_{qs}}{dt} - A \cdot \frac{d\lambda}{dt} \quad (8A)$$

Further manipulation leads to isolate the load angle derivative, leading to (9A), which is in turn the continuous time form of the key control equation (5).

$$\frac{d\delta}{dt} = \frac{\frac{di_{qs}}{dt} + \frac{L_q - L_d}{2 \cdot L_d \cdot L_q} \cdot \frac{d\lambda}{dt}}{\frac{\cos\delta}{L_d} \cdot \lambda_m - \frac{(L_q - L_d) \cdot \cos(2\delta)}{L_q \cdot L_d} \lambda} \quad (9A)$$

REFERENCES

[1] Burress, T.; Campbell, S., "Benchmarking EV and HEV power electronics and electric machines", Transportation Electrification Conference and Expo (ITEC), 2013 IEEE, pp. 1-6, 16-19 June 2013.

[2] EL-Refaie, A.M., "Fractional-Slot Concentrated-Windings Synchronous Permanent Magnet Machines: Opportunities and Challenges," Industrial Electronics, IEEE Transactions on, vol. 57, no. 1, pp. 107-121, Jan. 2010.

[3] Wenping Cao; Mecrow, B.C.; Atkinson, G.J.; Bennett, J.W.; Atkinson, D.J., "Overview of Electric Motor Technologies Used for More Electric Aircraft (MEA)," Industrial Electronics, IEEE Transactions on , vol.59, no.9, pp.3523,3531, Sept. 2012

[4] Tae-Suk Kwon; Gi-Young Choi; Mu-Shin Kwak; Seung-Ki Sul, "Novel Flux-Weakening Control of an IPMSM for Quasi-Six-Step Operation," Industry Applications, IEEE Transactions on , vol.44, no.6, pp.1722,1731, Nov.-dec. 2008

[5] Jahns, T.M., "Flux-Weakening Regime Operation of an Interior Permanent-Magnet Synchronous Motor Drive," Industry Applications, IEEE Transactions on , vol.IA-23, no.4, pp.681,689, July 1987

[6] Jang-Mok Kim; Seung-Ki Sul, "Speed control of interior permanent magnet synchronous motor drive for the flux weakening operation," Industry Applications, IEEE Transactions on , vol.33, no.1, pp.43,48, Jan/Feb 1997

[7] Pellegrino, G.; Vagati, A.; Guglielmi, P.; Boazzo, B., "Performance Comparison Between Surface-Mounted and Interior PM Motor Drives for Electric Vehicle Application," Industrial Electronics, IEEE Transactions on , vol.59, no.2, pp.803,811, Feb. 2012

[8] Buja, G.S.; Kazmierkowski, M.P., "Direct torque control of PWM inverter-fed AC motors - a survey," Industrial Electronics, IEEE Transactions on, vol. 51, no. 4, pp. 744- 757, Aug. 2004.

[9] Pellegrino, G.; Bojoi, R.I.; Guglielmi, P., "Unified Direct-Flux Vector Control for AC Motor Drives," Industry Applications, IEEE Transactions on, vol. 47, no. 5, pp. 2093-2102, Sept.-Oct. 2011.

[10] Inoue, Y.; Morimoto, S.; Sanada, M., "Control Method Suitable for Direct-Torque-Control-Based Motor Drive System Satisfying Voltage and Current Limitations," Industry Applications, IEEE Transactions on, vol. 48, no. 3, pp. 970-976, May-June 2012.

[11] J-S Lee; C-H Choi; J-K Seok; Lorenz, R.D., "Deadbeat-Direct Torque and Flux Control of Interior Permanent Magnet Synchronous Machines with Discrete Time Stator Current and Stator Flux Linkage Observer," Industry Applications, IEEE Trans. on, vol. 47, no. 4, pp.1749-1758, July-Aug. 2011.

[12] Boazzo, B.; Pellegrino, G., "Predictive direct flux vector control of Permanent Magnet Synchronous Motor drives," Energy Conversion Congress and Exposition (ECCE), 2013 IEEE , vol., no., pp.2086,2093, 15-19 Sept. 2013

[13] Bolognani, S.; Calligaro, S.; Petrella, R., "Adaptive Flux-Weakening Controller for Interior Permanent Magnet Synchronous Motor Drives," Emerging and Selected Topics in Power Electronics, IEEE Journal of , vol.2, no.2, pp.236,248, June 2014

[14] Pellegrino, G.; Bojoi, R.I.; Guglielmi, P.; Cupertino, F., "Accurate Inverter Error Compensation and Related Self-Commissioning Scheme in Sensorless Induction Motor Drives," Industry Applications, IEEE Transactions on, vol. 46, no. 5, pp. 1970-1978, Sept.-Oct. 2010.

[15] Jong-Woo Choi; Seung-Ki Sul, "Inverter output voltage synthesis using novel dead time compensation," Power Electronics, IEEE Transactions on , vol. 11, no. 2, pp. 221,227, Mar 1996

[16] Piippo, A.; Hinkkanen, M.; Luomi, J., "Adaptation of Motor Parameters in Sensorless PMSM Drives," Industry Applications, IEEE Transactions on , vol.45, no.1, pp.203,212, Jan.-feb. 2009

[17] Reddy, P.B.; EL-Refaie, A.M.; Kum-Kang Huh; Tangudu, J.K.; Jahns, T.M., "Comparison of Interior and Surface PM Machines Equipped With Fractional-Slot Concentrated Windings for Hybrid Traction Applications," Energy Conversion, IEEE Trans. on, vol. 27, pp. 593-602, Sept. 2012.

[18] Maes, J.; Melkebeek, J., "Discrete time direct torque control of induction motors using back-EMF measurement," Industry Applications Conference, 1998. Thirty-Third IAS Annual Meeting. The 1998 IEEE , vol.1, no., pp.407,414 vol.1, 12-15 Oct. 1998

[19] Abu-Rub, H.; Guzinski, J.; Krzeminski, Z.; Toliyat, H. A., "Predictive current control of voltage source inverters," Industrial Electronics Society, 2001. IECON '01. The 27th Annual Conference of the IEEE , vol.2, no., pp.1195,1200 vol.2, 2001

[20] Bolognani, S.; Petrella, R.; Prearo, A.; Sgarbossa, L., "Automatic Tracking of MTPA Trajectory in IPM Motor Drives Based on AC

Current Injection," Industry Applications, IEEE Transactions on, vol. 47, no. 1, pp. 105-114, Jan.-Feb. 2011.

[21] K. Rahman and S. Hiti "Identification of machine parameters of a synchronous motor", IEEE Trans. Ind. Appl. , vol. 41, no. 2, pp. 557 -565 2005

[22] Armando, E.; Bojoi, R.I.; Guglielmi, P.; Pellegrino, G.; Pastorelli, M., "Experimental Identification of the Magnetic Model of Synchronous Machines," Industry Applications, IEEE Transactions on, vol.49, no.5, pp.2116,2125, Sept.-Oct. 2013

[23] Pellegrino, G.; Boazzo, B.; Jahns, T.M.; "Magnetic Model Self-Identification for PM Synchronous Machine Drives," Optimization of Electrical and Electronic Equipment (OPTIM), 2014 14th International Conference on , 22-24 May 2014.